
This is an electronic reprint of the original article.
This reprint may differ from the original in pagination and typographic detail.

Akmal, Jan Sher; Macarie, Mihai; Björkstrand, Roy; Minet, Kevin; Salmi, Mika

Defect detection in laser-based powder bed fusion process using machine learning classification methods

Published in:
IOP Conference Series: Materials Science and Engineering

DOI:
[10.1088/1757-899X/1296/1/012013](https://doi.org/10.1088/1757-899X/1296/1/012013)

Published: 22/12/2023

Document Version
Publisher's PDF, also known as Version of record

Published under the following license:
CC BY

Please cite the original version:
Akmal, J. S., Macarie, M., Björkstrand, R., Minet, K., & Salmi, M. (2023). Defect detection in laser-based powder bed fusion process using machine learning classification methods. *IOP Conference Series: Materials Science and Engineering*, 1296, Article 012013. <https://doi.org/10.1088/1757-899X/1296/1/012013>

This material is protected by copyright and other intellectual property rights, and duplication or sale of all or part of any of the repository collections is not permitted, except that material may be duplicated by you for your research use or educational purposes in electronic or print form. You must obtain permission for any other use. Electronic or print copies may not be offered, whether for sale or otherwise to anyone who is not an authorised user.

PAPER • OPEN ACCESS

Defect detection in laser-based powder bed fusion process using machine learning classification methods

To cite this article: Jan Akmal *et al* 2023 *IOP Conf. Ser.: Mater. Sci. Eng.* **1296** 012013

View the [article online](#) for updates and enhancements.

You may also like

- [CNN-based classification of fNIRS signals in motor imagery BCI system](#)
Tengfei Ma, Shasha Wang, Yuting Xia et al.
- [Incorporating Measurement Error in Astronomical Object Classification](#)
Sarah Shy, Hyungsuk Tak, Eric D. Feigelson et al.
- [Classification methods to detect sleep apnea in adults based on respiratory and oximetry signals: a systematic review](#)
M B Uddin, C M Chow and S W Su

PRIME
PACIFIC RIM MEETING
ON ELECTROCHEMICAL
AND SOLID STATE SCIENCE

HONOLULU, HI
Oct 6-11, 2024

Abstract submission deadline:
April 12, 2024

Learn more and submit!

Joint Meeting of
The Electrochemical Society
•
The Electrochemical Society of Japan
•
Korea Electrochemical Society

Defect detection in laser-based powder bed fusion process using machine learning classification methods

Jan Akmal^{1,2}, Mihai Macarie³, Roy Björkstrand¹, Kevin Minet², Mika Salmi¹

1. Department of Mechanical Engineering, Aalto University, Puumiehenkuja 3, 02150 Espoo, Finland
2. EOS Metal Materials, Electro Optical Systems Finland Oy, Lemminkäisenkatu 36, 20520 Turku, Finland
3. Faculty of Electrical Engineering, Mathematics and Computer Science, University of Twente, Drienerlolaan 5, 7522 NB Enschede, The Netherlands

Email: jan.akmal@aalto.fi, jan.akmal-ext@eos.info

Abstract. The aim of this study is to deploy machine learning (ML) classification methods to detect defective regions in additive manufacturing, colloquially known as 3D printing, particularly for the laser-based powder bed fusion process. A custom-designed test specimen composed of 316L was manufactured using EOS M 290 machine. Multinomial logistic regression (MLR), artificial neural network (ANN), and convolutional neural network (CNN) classification techniques were applied to train the ML models using optical tomography infrared images of each additively manufactured layer of test specimen. Based on the trained MLR, ANN, and CNN classifiers, the ML models predict whether the manufactured layer is standard or defective, yielding five classes. Defective layers were classified into two classes for lack of fusion and two classes for keyhole porosity. The supervised approach yielded impeccable accuracy (>99%) for all three classification methods, however CNN inherited the highest degree of performance with 100% accuracy for independent test dataset unfamiliar to the model for unbiased evaluation. The high performance and low cost of computing observed in this work can have the potential to detect and eliminate defective regions by tuning the processing parameters in real time resulting in significantly decreased costs, lead-time, and waste. The proposed quality control can enable mass adoption of additive manufacturing technologies in a vast number of industries for critical components that are design- and shape- agnostic.

1. Introduction

Additive manufacturing (AM), colloquially known as 3D printing, is a novel and disruptive mode of manufacturing that allows creation of parts on a layer-by-layer basis using digital 3D model data [1]. The layer-by-layer mechanism of the additive process enables tool-less production of parts with unprecedented geometric freedom in one build cycle [2]. Comparatively, the subtractive process involves selective removal of material via a tool and formative process involves pressurizing a body of raw material into a mould to obtain a part [3]. In both cases, part-specific tools and moulds favour economies of scale and limit design freedom. On the other hand, the tool-less layer-by-layer mechanism is emerging into a general purpose technology akin to computers and dynamos serving a plethora of applications [4]. AM can be categorized into seven group of technologies [1] depending on the layer-wise addition and fusion mechanisms of feedstock material. Today, it is used for tooling [2,5],



prototyping [6,7], and end-use part [8–11] applications in a wide range of industries, e.g., medical, industrial machines, defence, automotive, and aerospace industries.

More specifically, the laser-based powder bed fusion (PBF-LB) process has been gaining traction within the industrial landscape to create lightweight metallic parts on demand [4,12] using generative design, topology optimization, and lattice formation [2,7]. During the PBF-LB process, the impinging laser energy selectively fuses regions of powder bed [2] to create the intended part on a layer-by-layer principle. The underlying process dynamics are complex and not fully understood [13]. The process is inherent to large thermal gradients, heat absorption, local melting and re-solidification of particles, phase change, plumes, spatter, and Marangoni convection [14]. To mitigate these inherent characteristics, the parts are manufactured using support structures for heat dissipation and anchoring the parts to the build platform [10].

Nevertheless, the process is highly sensitive to energy density, i.e., laser power, scan speed, hatch distance, and layer thickness, which can cause under- or over- heating. A slight deviation from the thresholded volumetric energy density caused by process and environment uncertainties can induce lack of fusion and keyhole porosity resulting in structural defects, i.e., porosity, support rupture, warpage, residual stresses, cracking, balling and geometric defects, in the part [15]. Further, the under- or over-heating can cause disturbances in powder bed, recoater crashes, and eventually premature failure of intended parts.

The aim of this study is to create PBF-LB process variation-dependent defective regions on a layer-by-layer basis and to use three machine learning (ML) methods for detection. This study overcomes the lack of understanding in the transitional phase of process parameters and temporal thermal fingerprint emitted during the process. This allows for engineering functional end-use parts by reducing the uncertainty in passing stringent quality standards and easing the widespread adoption in various applications in a wide range of precision industries.

2. Methods

2.1. Additive manufacturing

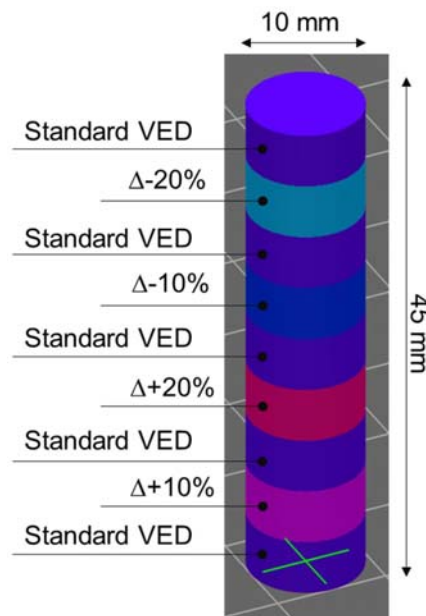
The EOS M 290 (EOS Gmbh, Krailling, Germany) machine was used to manufacture a tailor-made test specimen using the PBF-LB process. The volumetric energy density (VED) function is the critical independent variable for the design of experiment, which is formulated as follows:

$$VED = \frac{P_L}{v \times h \times L_t} \quad (1)$$

where P_L is the laser power [W], v is the exposure scan speed [mm/s], h is the hatch distance [mm], and L_t is the layer thickness [mm]. The design of experiment involving five volumetric energy densities is shown in Table 1. EOSTATE Exposure optical tomography (OT) monitoring system (EOS Gmbh, Krailling, Germany), comprising of a scientific complementary metal-oxide-semiconductor (sCMOS) sensor, was used to capture near-infrared images of each layer. The test specimen was manufactured using 316L as feedstock powder ($D_{v(25)}=24\mu\text{m}$, $D_{v(50)}=37\mu\text{m}$, $D_{v(75)}=56\mu\text{m}$) at the centre of the build platform using the EOS 316_SurfaceM291_1.10 parameter set. Argon was used as inert shielding gas. Table 1 shows the number of OT images as a function of exposure nomenclature for hatch infill adopted in this study. The test specimen and the segmented exposure strategies are shown in Figure 1. Owing to such a small selectively melted cross-section region per layer of the build, a minimum exposure time of 18 s was added to ensure the likelihood of a successful print.

Table 1. Additive manufacturing parameters

Exposure Nomenclature	Power [W]	Scan speed [mm/s]	Hatch Distance [mm]	Layer Thickness [mm]	Energy Density [J/mm ³]	No. of OT Images [-]
Δ -20% VED	156	1083	0.09	0.02	80.02	249
Δ -10% VED	175.5	1083	0.09	0.02	90.03	247
Standard VED	195	1083	0.09	0.02	100.03	1248
Δ +10% VED	214.5	1083	0.09	0.02	110.03	249
Δ +20% VED	234	1083	0.09	0.02	120.04	247

**Figure 1.** Dimensions and exposure strategies of the test specimen.

2.2. Machine learning

2.2.1. Dataset. The data comprises of 2238 OT images in JPG format after removing the first ten and the last two OT images owing to the variation in the light emissions. For the first ten layers, the variation can be caused by for example reduced layer thickness of first layer, reflectivity of the build platform, and double exposure of the first two layers. For the last two layers, the variation is caused by up-skin parameters. Each image represents process radiation in the near infrared spectrum of the laser-based selectively melted layer over the entire build platform. Each image corresponds to the thermal history of one layer. The original dimension of each image is 2000 x 2000 pixels. After visualizing the dataset, the insignificant regions of the OT images were removed. Subsequently, each OT image is cropped to focus on the region of interest resulting in 100 x 100 pixels (width x height) and 10000 pixel squared. Each pixel represents a shade of grey as a 24-bit integer (range 0-255). The number of OT images as a function of exposure nomenclature are shown in Table 1.

2.2.2. Features. This study uses deep learning in which features of each OT image can be depicted as a vector $\mathbf{x}^i \in \mathbb{R}^{10000}$ composed of integers, where every i -th entry represents a grayscale value in the range of 0 to 255. A grayscale value of 0 depicts black and 255 denotes white. Further, OT images were

mapped with RYB colour model for visualization. To assist the activation function in deep learning, this range is normalized between 0 and 1 [16]. Each image corresponds to the 100 x 100 tensor format containing multidimensional feature input. The first 100 entries of the feature vector depict the top row of each OT image, the second 100 entries denote the second row from top, and similarly the remaining entries are filled until the bottom-most row with an index of 100. This is the prescribed tensor format for Tensorflow [16] which is adopted in this work.

2.2.3. Labels. The label of each datapoint, i.e., each OT image, is a multi-class classification, $y \in \{0,1,2,3,4\}$, denoting a Δ -10% VED layer $\hat{y}^i = 0$, a Δ -20% VED layer $\hat{y}^i = 1$, a Δ +10% VED layer $\hat{y}^i = 2$, a Δ +20% VED layer $\hat{y}^i = 3$, and a Standard VED layer $\hat{y}^i = 4$. Supervised approach is used to manually label the datapoints yielding five classes.

2.2.4. Classification methods. This study adopts three ML classification methods, i.e., multinomial logistic regression (MLR), artificial neural network (ANN), and convolutional neural network (CNN), to classify five classes of OT images as shown in Table 1. Open-source Jupyter Notebook (6.4.8, Project Jupyter) operating on Python (3.9.12, Python Software Foundation) was used to build the architecture of the ML models using an off-the-shelf mobile workstation.

The MLR applies the parameters of the linear map $h(x)=w^T x$ that classifies datapoints, i.e., OT images, into label value \hat{y}^i . Sparse categorical cross-entropy loss is used to quantify the performance of the linear map because the five label classes comprise of integers. A dense layer (fully connected layer) is created with 5 neurons. Softmax is used to transform logits to valid probabilities [16].

The ANN architecture is built on a feedforward neural network that classifies datapoints, i.e., OT images, into label value \hat{y}^i . In this case, two dense layers, comprising of 2048 and 5 neurons respectively, are created with rectified linear unit (ReLU) as an activation function. Further, a dropout layer (regularization layer) is added with a rate of 0.2 to prevent overfitting. The model also uses sparse categorical cross-entropy as the loss function.

Finally, the CNN architecture adopts a feedforward neural network that classifies datapoints, i.e., OT images, into label value \hat{y}^i . It consists of a convolutional base, which includes convolutional layers (i.e., spatial convolutional over each OT image), and pooling layers (i.e., to produce lower resolution of the feature map) [17]. Finally, two dense layers, comprising of 64 and 5 neurons respectively, are added to perform classification using ReLU. Sparse categorical cross-entropy loss is used to quantify the performance of the network.

2.2.5. Data splitting. For this supervised approach, OT images were manually sorted into five classes, $y \in \{0,1,2,3,4\}$, as shown in Table 1. The dataset is randomly split in a manner that represents 70% for training the ML models and 20% for validating them. This means 1571 OT images are used to train the ML models and 442 OT images are used for validating. The remaining 10% of the dataset were used for testing the ML models. The five classes were split identically, representing similar percentages. This training, validation, and testing ratio is within the range suggested by empirical studies obtaining the optimal results [18].

3. Results and discussion

The additively manufactured test specimen with segmented exposure strategies according to Figure 1 is shown in Figure 2. When observed closely, the segmentation regions are visible on the surface of the manufactured test specimen. A highlight of processed OT image for each VED is shown in Figure 3.



Figure 2. Additively manufactured test specimen (316L) with segmented exposure strategies.

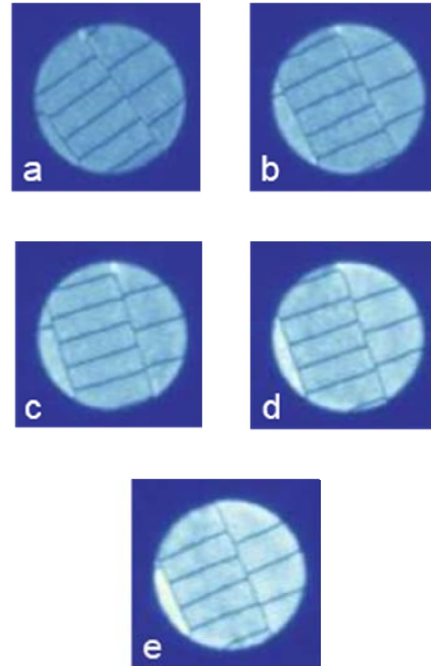


Figure 3. A processed OT image for a) Δ -20%, b) Δ -10%, c) Standard, d) Δ +10%, and e) Δ +20% VED layers.

The accuracy and loss functions of MLR, ANN, and CNN are shown in Figure 4. The MLR model was able to obtain a 100% training and validation accuracy at the 57th epoch with loss values of 0.026 and 0.035 respectively. Comparatively, the CNN model was able to achieve 100% training and validation accuracy at the 5th epoch with loss of 0.007 and 0.004. On the other hand, the ANN model was not able to converge training and validation accuracy to a value of 100%. In this case, the highest values observed were 96% for training and 98% for validation with 0.146 and 0.081 as loss values. As depicted in Figure 5, the CNN model was able to train and validate the model 42% faster than MLR and 66% faster than ANN.

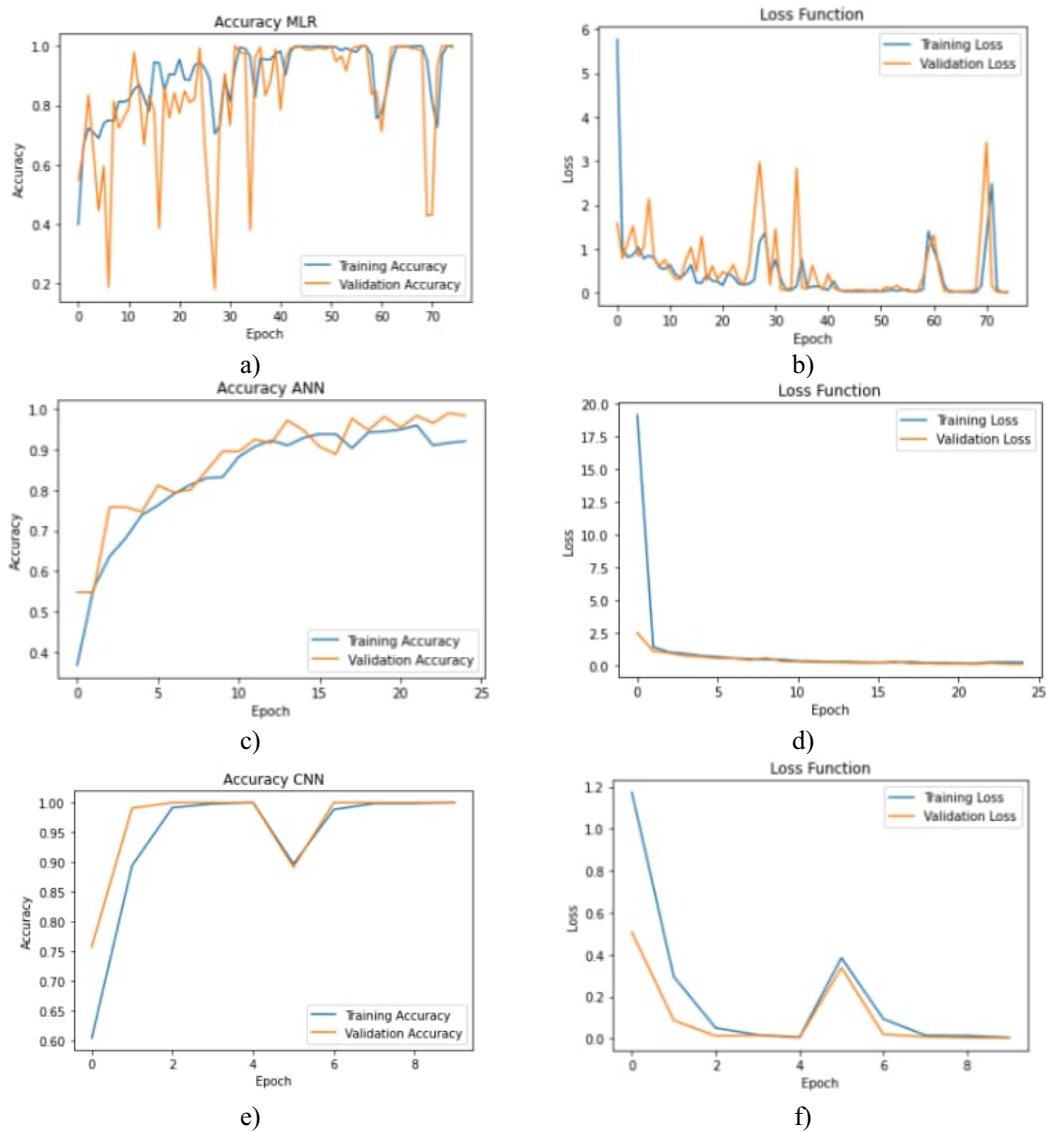


Figure 4. Accuracy as a function of epoch for a) MLR, c) ANN, and e) CNN, and results of loss function with respect to epoch for b) MLR, d) ANN, and f) CNN.

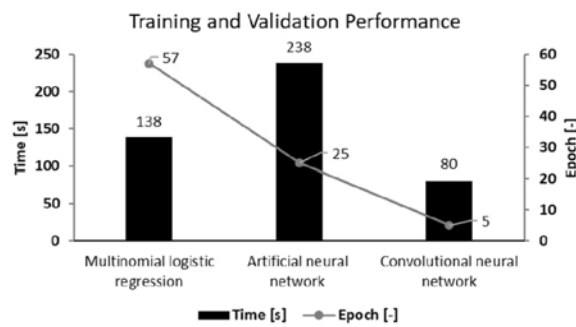


Figure 5. Training and validation performance of the ML models.

Confusion matrices of each ML classification method for test dataset are shown in Figure 6. As observed from Figure 6a and 6c, the MLR and CNN models yielded impeccable accuracy of 100% for evaluating the test dataset. Considering that the test dataset was not used for training nor validating the ML models, this is a remarkable outcome. The loss values for MLR and CNN were 0.023 and 0.002 respectively. In contrast, the ANN model yielded 99.6% accuracy for the test dataset with a loss value of 0.082. As observed from Figure 6b, the ANN model predicted one $\Delta+10\%$ (Pos-10) VED layer as Standard VED layer. The testing performance of each ML model is denoted in Figure 7.

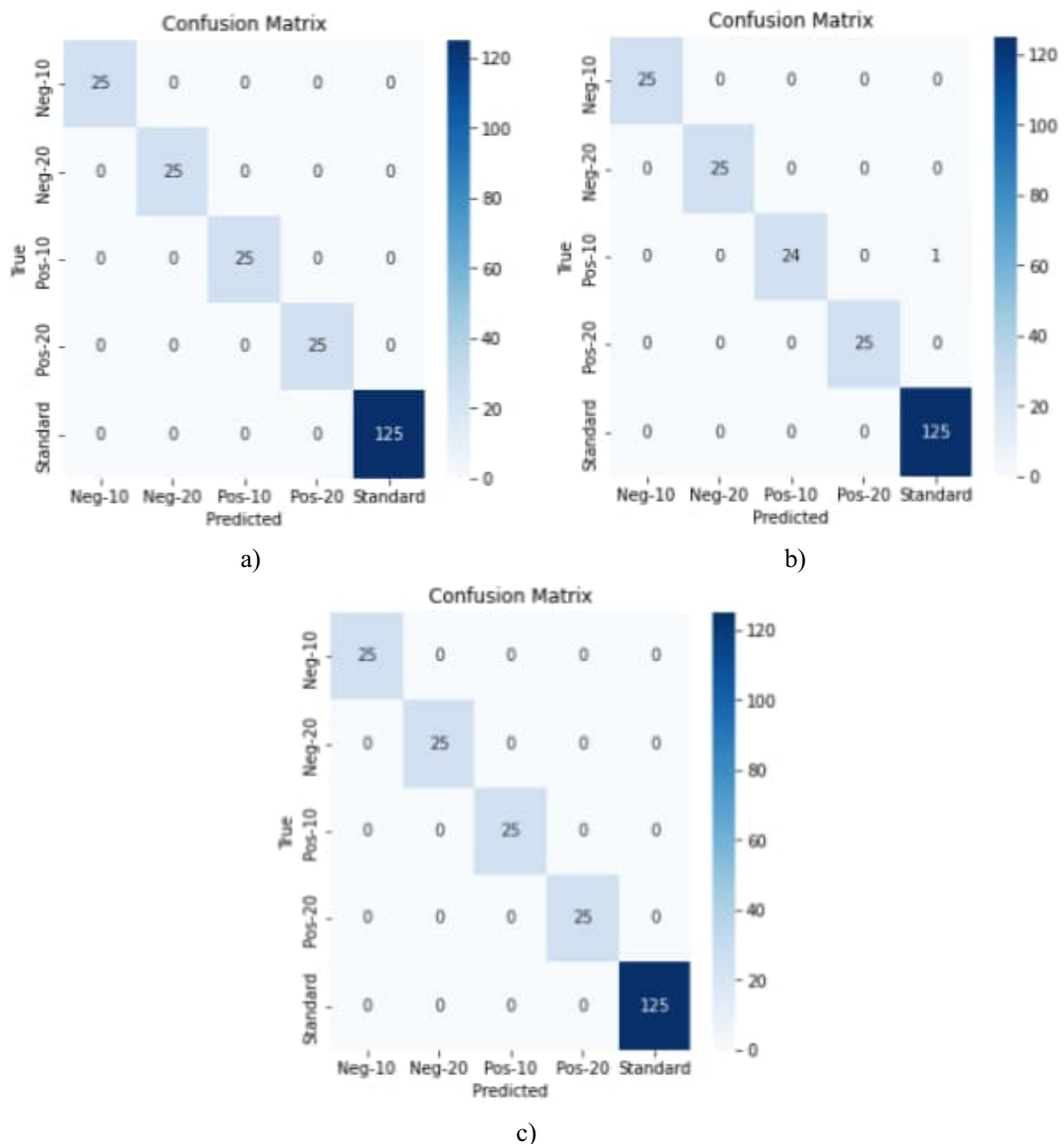


Figure 6. Confusion matrix of a) MLR, b) ANN, and c) CNN models for test dataset.

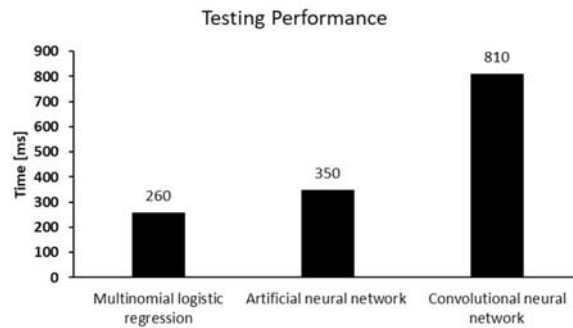


Figure 7. Testing performance of the ML models.

Extant literature has identified that a slight deviation from the thresholded VED can induce structural defects in the part [13,19–22]. This is also evidenced in this study as shown in Figure 8, which includes micrographs of polished cross-section with a magnification of 3.15x, highlight of OT images and their mean gray values as a function of each exposure strategy (Figure 1) in the build direction (Z-height).

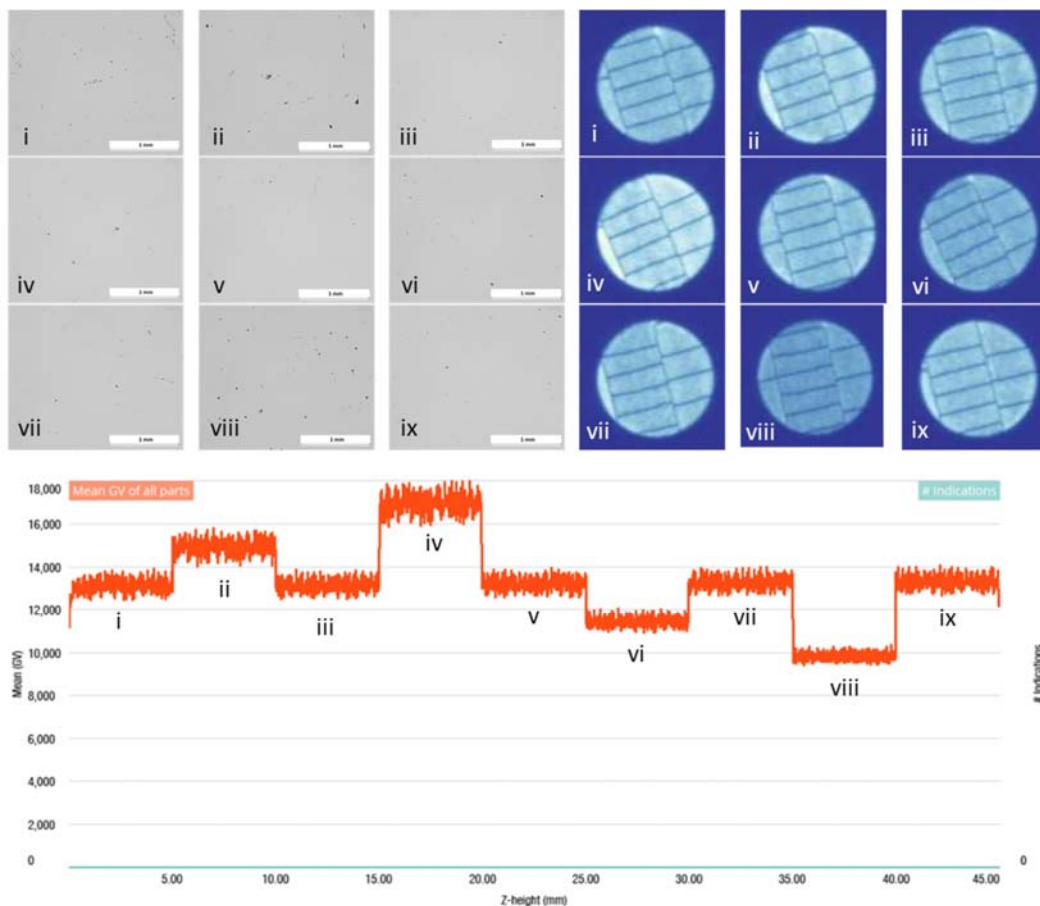


Figure 8. Micrograph (3.15x), OT image, and mean gray values of each exposure strategy in the build direction of the test specimen.

This study created defective regions using build parameter manipulation that are concomitant to lack of fusion and keyhole porosity. Two classes of keyhole porosity were created by an increase in Standard VED by 10% (Figure 8*ii*) and 20% (Figure 8*iv*). Similarly, two classes of lack of fusion were created by a reduction in Standard VED by 10% (Figure 8*vi*) and 20% (Figure 8*viii*). Generally, the micrographs presented in Figure 8 yielded higher defect percentage for deviated VED compared to the preceding Standard VED. The Δ -20% VED yielded the highest defect percentage of 0.24% compared to the average Standard VED defect percentage of 0.096% observed in this study. Additional samples representing a statistically sound dataset should be collected for conclusive outcome. Compared to the literature [13,22–24], this study develops and evaluates the accuracy and performance of three ML classification methods for detecting four defective classes and one standard class. The outcome confirms high performance (up to 100% accuracy) for training, validation, and test datasets. No indications of over- or under- fitting were observed because the validation error was similar to the training error. The high speed of detection (within 100s of millisecond for test dataset of 225 OT images) observed in this study enables opportunities to detect defective regions in real time and even compensate them in the current or subsequent layers by tuning the VED using a closed feedback loop. Considering such a high performance outcome for detecting layer-based defective regions with conventional computing power, this study opens opportunities to detect multiple vector-based defective regions in real-time for future work. Future studies should focus on further destructive and non-destructive testing for verifying the degree of defect generation and compensation also considering the degree of self-healing phenomena.

4. Conclusion

Additive manufacturing is shifting towards general-purpose manufacturing technology analogous to dynamos and computers that offer a vast number of applications in a wide range of industries. However, uncertainty in passing stringent quality standards hinders its adoption. To assist this transition, this study leverages the layer-by-layer mechanism of PBF-LB to develop three ML classification methods to detect defective regions inside the parts. A tailor-made test specimen is additively manufactured with five segmented exposure strategies emulating defective regions composed of two classes of lack of fusion and two classes of keyhole porosity. The artificial intelligence-based classifiers yielded flawless accuracy (up to 100% accuracy for MLR and CNN) for classifying OT images of each exposure strategy composed of independent test dataset for unbiased evaluation metrics. The high performance and low cost of computing of this layer-based approach opens a direction for detecting and compensating scan-based anomalies in real time for shifting the paradigm of uncertainty in quality of additively manufactured parts.

Funding: This research has been executed with Tandem Industry Academia funding from the Finnish Research Impact Foundation.

Conflict of interest: The authors declare no conflict of interest.

Acknowledgements: Special acknowledgements are extended to Harald Krauss, Jouni Partanen, Olli Nyrhilä, Tatu Syvänen, Pilvi Ylander, and Niko Raitanen for valuable discussions.

References

1. ISO/ASTM 52900. ISO/ASTM 52900:2021(en) Additive Manufacturing - General principles - Terminology. 2nd ed. ISO/ASTM International 2015; 2021.
2. Akmal JS. Digital Unique Component Manufacturing Through Direct and Indirect Additive Manufacturing [Internet]. Aalto University; 2017. Available from: <https://aaltodoc.aalto.fi/handle/123456789/28509>
3. Akmal JS. Switchover to additive manufacturing: Dynamic decision-making for accurate,

- personalized and smart end-use parts [Internet]. Aalto University; 2022. Available from: <http://urn.fi/URN:ISBN:978-952-64-1013-5>
4. Akmal JS, Salmi M, Björkstrand R, Partanen J, Holmström J. Switchover to industrial additive manufacturing: dynamic decision-making for problematic spare parts. *Int J Oper Prod Manag.* 2022;42(13):358–84.
 5. Salmi M, Partanen J, Tuomi J, Chekurov S, Björkstrand R, Huotilainen E, et al. Digital spare parts [Internet]. 2018. Available from: <http://urn.fi/URN:ISBN:978-952-60-3746-2>
 6. Akmal JS, Salmi M, Mäkitie A, Björkstrand R, Partanen J. Implementation of industrial additive manufacturing: Intelligent implants and drug delivery systems. *J Funct Biomater.* 2018 Jun 29;9(3):41.
 7. Wohlers. Wohlers Report. Colorado: Wohlers Associates Inc.; 2021.
 8. Kukko K, Akmal JS, Kangas A, Salmi M, Björkstrand R, Viitanen AK, et al. Additively manufactured parametric universal clip-system: An open source approach for aiding personal exposure measurement in the breathing zone. *Appl Sci.* 2020;10(19):6671.
 9. Salmi M, Akmal JS, Pei E, Wolff J, Jaribion A, Khajavi SH. 3D printing in COVID-19: Productivity estimation of the most promising open source solutions in emergency situations. *Appl Sci* [Internet]. 2020 Jun 9;10(11):4004. Available from: <https://www.mdpi.com/2076-3417/10/11/4004>
 10. Akmal JS, Salmi M, Hemming B, Teir L, Suomalainen A, Kortensniemi M, et al. Cumulative inaccuracies in implementation of additive manufacturing through medical imaging, 3D thresholding, and 3D modeling: A case study for an end-use implant. *Appl Sci* [Internet]. 2020 Apr 24;10(8):2968. Available from: <https://www.mdpi.com/2076-3417/10/8/2968>
 11. Ullah R, Lian J, Akmal J, Wu J, Niemi E. Prediction and validation of melt pool dimensions and geometric distortions of additively manufactured AlSi10Mg. *Int J Adv Manuf Technol* [Internet]. 2023;(0123456789). Available from: <https://doi.org/10.1007/s00170-023-11264-w>
 12. Oettmeier K, Hofmann E. Impact of additive manufacturing technology adoption on supply chain management processes and components. *J Manuf Technol Manag* [Internet]. 2016 [cited 2021 May 19];27(7):944–68. Available from: <https://www.emerald.com/insight/content/doi/10.1108/JMTM-12-2015-0113/full/html>
 13. Wang P, Yang Y, Moghaddam NS. Process modeling in laser powder bed fusion towards defect detection and quality control via machine learning: The state-of-the-art and research challenges. *J Manuf Process* [Internet]. 2022;73(November 2021):961–84. Available from: <https://doi.org/10.1016/j.jmapro.2021.11.037>
 14. Soundararajan B, Sofia D, Barletta D, Poletto M. Review on modeling techniques for powder bed fusion processes based on physical principles. *Addit Manuf* [Internet]. 2021;47(April):102336. Available from: <https://doi.org/10.1016/j.addma.2021.102336>
 15. Bauereiß A, Scharowsky T, Körner C. Defect generation and propagation mechanism during additive manufacturing by selective beam melting. *J Mater Process Technol* [Internet]. 2014;214(11):2522–8. Available from: <http://dx.doi.org/10.1016/j.jmatprotec.2014.05.002>
 16. Abadi M, Agarwal A, Barham P, Brevdo E, Chen Z, Citro C, et al. TensorFlow: Large-Scale Machine Learning on Heterogeneous Distributed Systems. 2016 Mar 14 [cited 2022 Oct 8]; Available from: <https://arxiv.org/abs/1603.04467>
 17. Albawi S, Mohammed TA, Al-Zawi S. Understanding of a convolutional neural network. *Proc 2017 Int Conf Eng Technol ICET 2017.* 2018;2018-Janua:1–6.
 18. Gholamy A, Kreinovich V, Kosheleva O. Why 70/30 or 80/20 Relation Between Training and Testing Sets : A Pedagogical Explanation. *Dep Tech Reports.* 2018;1–6.
 19. Luo Q, Yin L, Simpson TW, Beese AM. Effect of processing parameters on pore structures, grain features, and mechanical properties in Ti-6Al-4V by laser powder bed fusion. *Addit Manuf* [Internet]. 2022;56(February):102915. Available from: <https://doi.org/10.1016/j.addma.2022.102915>
 20. Gong H, Rafi K, Gu H, Starr T, Stucker B. Analysis of defect generation in Ti-6Al-4V parts

- made using powder bed fusion additive manufacturing processes. *Addit Manuf* [Internet]. 2014;1:87–98. Available from: <http://dx.doi.org/10.1016/j.addma.2014.08.002>
21. ISO/ASTM/TR 52906. Additive manufacturing. Non-destructive testing. Intentionally seeding flaws in metallic parts (ISO/ASTM/TR 52906:2022). 2022.
 22. Schwerz C, Nyborg L. A neural network for identification and classification of systematic internal flaws in laser powder bed fusion. *CIRP J Manuf Sci Technol* [Internet]. 2022;37:312–8. Available from: <https://doi.org/10.1016/j.cirpj.2022.02.010>
 23. Baumgartl H, Tomas J, Buettner R, Merkel M. A deep learning-based model for defect detection in laser-powder bed fusion using in-situ thermographic monitoring. *Prog Addit Manuf* [Internet]. 2020;5(3):277–85. Available from: <https://doi.org/10.1007/s40964-019-00108-3>
 24. Kunkel MH, Gebhardt A, Mpofu K, Kallweit S. Quality assurance in metal powder bed fusion via deep-learning-based image classification. *Rapid Prototyp J*. 2020;26(2):259–66.